Article

New Compact Antenna Array for MIMO Internet of Things Applications

Wazie M. Abdulkawi [1,2,*] , **Mohammed A. Alqaisei** [1], **Abdel-Fattah A. Sheta** [1] **and Ibrahim Elshafiey** [1]

1   Electrical Engineering Department, King Saud University, Riyadh 11421, Saudi Arabia
2   Department of Electrical Engineering, College of Engineering in Wadi Addawasir,
    Prince Sattam bin Abdulaziz University, Wadi Addawasir 11991, Saudi Arabia
*   Correspondence: walkadri@ksu.edu.sa

Abstract: A communication system is proposed for the Internet of Things (IoT) applications in desert areas with extended coverage of regional area network requirements. The system implements a developed six-element array that operates at a 2.45 GHz frequency band and is optimized to reduce the size and limit element coupling to less than -20 dB. Analysis of the proposed system involves a multiple-input multiple-output (MIMO) operation to obtain the diversity gain and spectral efficiency. In addition, the radiation efficiency of the proposed antenna is greater than 65% in the operation bandwidth (more than 30 MHz) with a peak of 73% at 2.45 GHz. Moreover, an adaptive beamforming system is presented based on monitoring the direction of arrival (DOA) of various signals using the root MUSIC algorithm and utilizing the DOA data in a minimum variance distortionless response (MVDR) technique beamformer. The developed array is found to have an envelope correlation coefficient (ECC) value of less than 0.013, mean effective gain (MEG) of more than 1 dB, diversity gain of more than 9.9 dB, and channel capacity loss (CCL) of less than 0.4 bits/s/Hz over the operation bandwidth. Adaptive beamforming is used to suppress interference and enhance the signal-to-interference noise ratio (SINR) and is found to achieve a data rate of more than 50 kbps for a coverage distance of up to 100 km with limited power signals.

Keywords: Internet of Things (IoT); regional area network; multiple-input multiple-output (MIMO) antenna; channel capacity loss (CCL); MVDR beamforming; DOA estimation

1. Introduction

The Internet of Things (IoT) provides a paradigm of physical items equipped with software tools to achieve efficient data exchange among various devices. The challenges of IoT systems depend on the nature of the application. In applications related to rural and desert areas, the system typically involves sensing units that are distributed over large areas. Being operated with batteries or solar energy sources, the units should limit power use to reduce maintenance costs. The system also connects to a node that is connected to a cellular network, which can be tens of kilometers away, to make acquired data available on the internet to monitoring and control centers [1,2]. In [3,4] the monopole UWB antennas for IoT applications were proposed and designed with an inside cut-feed structure and linearly tapered transmission line, respectively.

IoT systems thus depend on a high level of intelligence to optimize system performance in a challenging environment. Part of the system intelligence can be achieved by using efficient and adaptive beamforming capability associated with the use of multiple-input multiple-output (MIMO) antenna arrays [5–8]. MIMO systems offer various advantages, including an increase in the data rate, enhancement of spectral efficiency, and boosting the diversity gain [9–11]. These systems provide higher capacity gain and are more robust to noise and fading channel conditions, allowing for larger data rates without sacrificing additional airwaves or transmission power [12,13].

The critical issues when building an antenna array for MIMO systems include a small distance between the antenna elements, compact size, low ECC, high isolation, and high efficiency [14–17]. Higher channel capacity can be accomplished by increasing the number of antenna elements [18]. The MIMO antenna elements are placed very close which causes mutual coupling which means reducing the MIMO system performance. As a result, the mutual coupling between the antenna elements remains the core issue [19,20]. Various decoupling approaches are presented and investigated in the literature to improve isolation [21,22].

In [23], 2×2 and 4×4 MIMO antenna systems were reported with wideband characteristics. The reported MIMO antennas were decoupled using the neutralization technique, in which a neutralization line is connected between the adjacent elements. This resulted in the isolation of < -22 dB and < -23 dB for 2×2 and 4×4, respectively. Similarly in [24], the dummy elements-decoupling isolation technique provided isolation of < -20 dB between the adjacent antenna elements. However, the size of the reported antenna was relatively large which was 44 mm. The reported design can enhance mutual coupling of the antenna, which boosts and enhance the performance efficiency of the antenna. In [25], a dual-band 4×4 MIMO antenna system was proposed in which the self-decoupled antenna technique was used. The proposed MIMO antenna system operated on 3.4–3.6 GHz and 4.8–5.0 GHz with isolation better than -17 dB for the low band and -20 dB for the high band. A multi-slot decoupling technique was proposed [26], in which a dual-band MIMO antenna system was designed. This system operated on 3.4–3.8 GHz and 4.8–5.0 GHz, giving isolation of -15.5 dB and -19 dB (-6 dB), respectively. The multi-slot structure is introduced to reduce mutual coupling between the antenna elements. In the reported work [27], an eight-element MIMO antenna array was proposed to cover 2.4–3.6 GHz bandwidth. The microstrip feeding-line decoupling technique was applied which gives -15 dB isolation and better channel capacity.

MIMO and beamforming techniques are the key enablers of enhanced connectivity and increased data rate. The beamforming technology is used to divert the radiations towards the desired direction and avoid them in unwanted directions. In other words, beamforming is used to focus the beam in the desired direction and cancel the undesirable signals and reduce the side lobe effect [28,29].

This paper proposes a MIMO-slotted square-patch antenna array, that was developed to be low-cost and small enough to be used in IoT applications and devices. This antenna can cover some IoT wireless standards, such as Bluetooth, Bluetooth smart (BLE), WiFi, and ZigBee.

The array has a reconfigurable architecture that allows it to operate in either receive or broadcast mode at the desired frequency.

The proposed antenna configuration is designed to operate in the industrial science medical band (ISM-band). Two prototypes are presented to be adopted for IoT applications at 2.45 GHz. The first configuration has only one element of the slotted square-patch antenna, however the second one has a six-element array of the proposed antenna. The single and MIMO antennas are designed, fabricated, and measured. The measured results correlate well with the simulated ones. Each antenna operates in the desired frequency band of operation with the minimum acceptable isolation of (≤ -20 dB) and ECC less than 0.2 for any two antennas of the array. Since the proposed solution can have a compact and low profile antenna structure, which has very good isolation and ECC value, it is very promising for practical IoT MIMO applications. After that, the beamforming function is analyzed based on the proposed array to show the potential of the developed array in enhancing signal-to-interference noise ratio (SINR), by suppressing unwanted interference.

In addition, the paper provides a simulation analysis of the proposed antenna in the typical IoT communication system to investigate the diversity gain (DG), capacity, and beamforming capabilities.

The study is scheduled as follows. A single element of the slotted square patch antenna is discussed in Section 2. In Section 3, the antenna array is designed and explained.

The array parameters and MIMO performance are discussed in Sections 4 and 5. The beamforming capabilities of the proposed array are shown in Section 6. In Section 7, the performance of the proposed communication system in the regional area network is discussed. The conclusions and discussions are presented in Section 8.

2. Single Element Antenna

Figure 1 illustrates the proposed slotted square-patch antenna (Ant 1). The antenna is designed as a microstrip square patch, along with etched four slots along the *X*- and *Y*-axes. All of the slots are of the same length and width [30]. The slotted square patch can be designed based on the fractal concept [31–34] or TM_{mn0} modes [35,36]. The latter is adopted and considered as a square cavity with magnetic walls. The field inside the square cavity matches those of the TM^z_{mn0} modes. The coherent modes (TM^z_{mn0}) and the resonance frequencies of the square-patch type can be calculated using the same way as described in [37–39]. In our case, the proposed structure is based on TM_{010} and TM_{100} modes. Only one mode (TM_{010}) is excited in the band of interest.
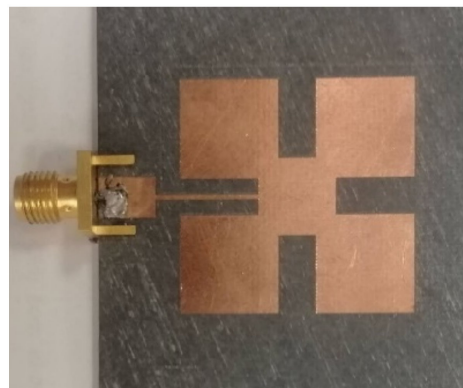

Figure 1. Single antenna element (Ant 1). The patch dimensions are optimized to operate at the 2.45 GHz frequency as: patch length and width = 28 mm, slot length = 9.3 mm, and slot width = 4.5 mm.

The antenna element is printed on the front surface of an RT Duroid 5880 dielectric substrate with relative permittivity of 2.2 and a loss tangent of 0.0009. The xyz dimensions are $41.5 \times 38.5 \times 1.57$ mm^3. The antenna is designed and optimized using full-wave electromagnetic computer simulation technology (CST Ver.2021).

Following the mathematical formulas described in [30,37–39], the primary antenna configuration resonating at 2.45 GHz is designed and fabricated. The fabricated prototype antenna is connected to a 50-ohm SMA connecter. The reflection coefficient (S_{11}) and radiation pattern at 2.45 GHz of Ant-1 are shown in Figures 2 and 3, respectively.
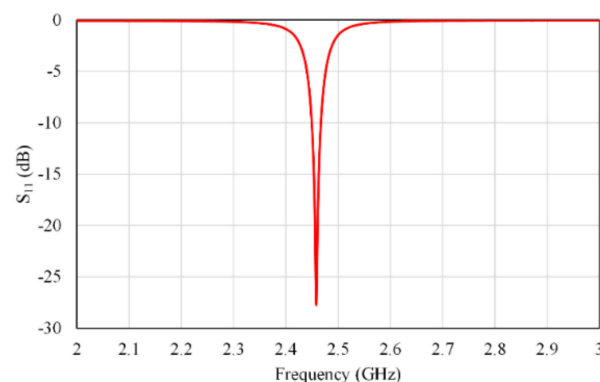

Figure 2. S_{11} response of a single antenna element; patch length and width = 28 mm, slot length = 9.3 mm, and slot width = 4.5 mm.
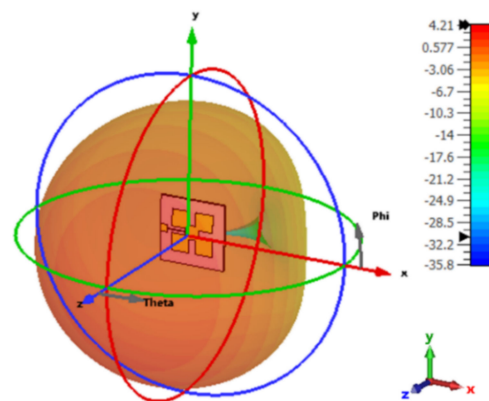
Figure 3. The simulated 3D radiation pattern of Ant 1.

Figure 4 shows the efficiency of the proposed single antenna. It is observed from this figure that the efficiency is greater than 65% in the operation bandwidth with a peak of 73% at 2.45 GHz.
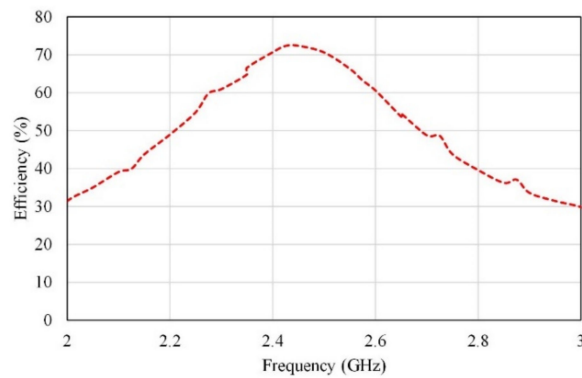

Figure 4. The efficiency of a single antenna element.

3. Proposed Array Structure

The proposed design is further processed from a single element to a two-element array, as shown in Figure 5.
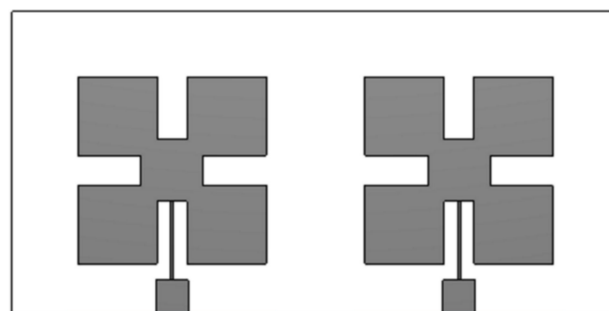

Figure 5. The two-element array of Ant 1.

The configuration has proceeded further to develop the three-port and four-port arrays. Finally, a fully grounded six-port array is developed, as shown in Figure 6, where six patch elements are printed on the top side of the Rogers substrate. The overall size of the antenna system is $97 \times 150 \times 1.6$ mm^3. Each element of the designed MIMO system is excited through a 50 ohm SMA connector.
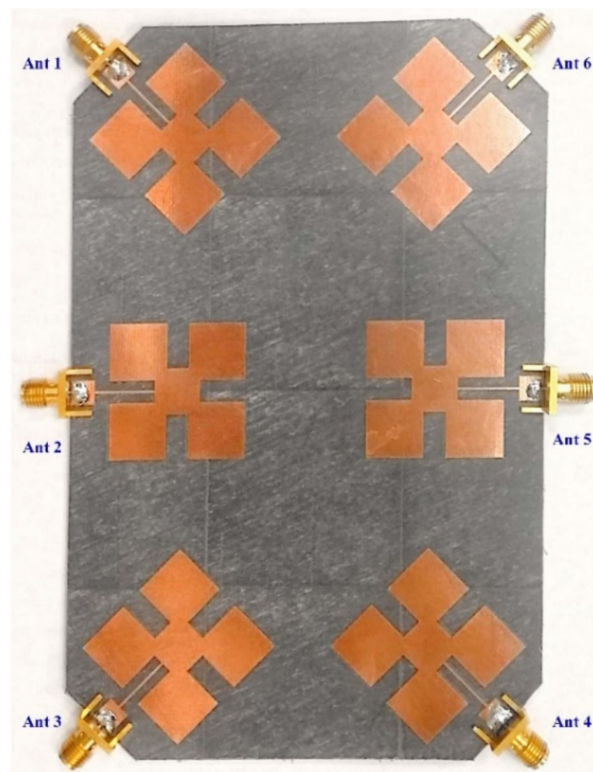
Figure 6. Photograph of the fully grounded proposed MIMO antenna array.

Increasing the mutual coupling reduces the isolation which adversely affects the performance of the antenna, and therefore it is difficult to achieve a low mutual coupling within a compact size in the design of the MIMO array antenna system [40–42]. In the proposed design, we increase the separation between two adjacent antennas in the proposed MIMO to around 25 mm (about a quarter wavelength) to obtain high isolation between the antenna elements. In addition, to achieve compactness, the antennas (Ant 1-Ant 6) are arranged in the manner shown in Figure 6. The simulated S-parameters of the proposed six-port antenna are shown in Figure 7.
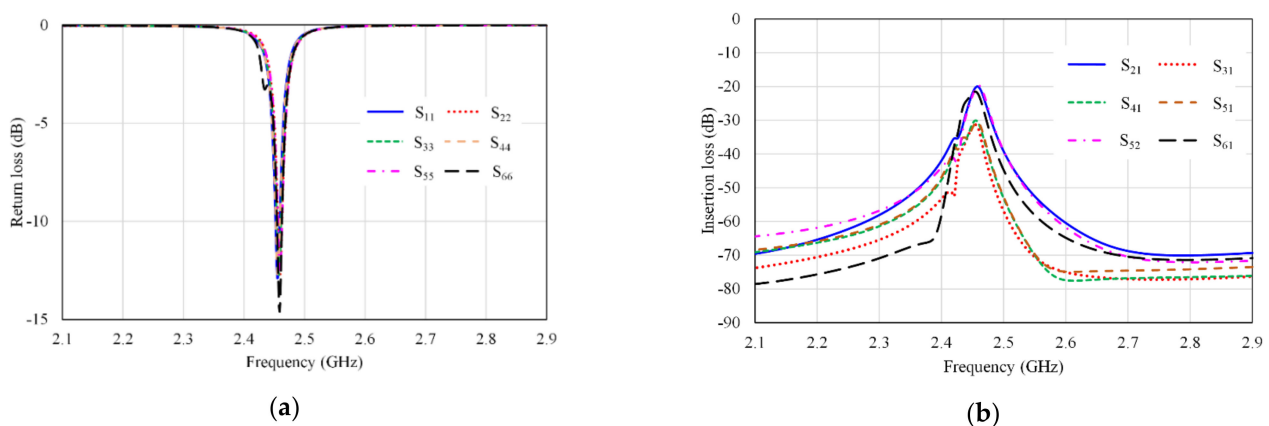

(**a**)

(**b**)

Figure 7. S-parameters for the six-port MIMO antenna array (**a**) return loss (S_{ii}), and (**b**) insertion loss (S_{ij}).

In Figure 7a, the reflection coefficients S_{ii} (i = 1, 2, . . . , 6) are almost identical. It is observed from the results in Figure 7b that the isolations between antenna elements represented by S_{ij} (i = 1, 2, . . . , 6, and j = 1, 2, . . . , 6, I $\neq$ j) are less than -20 dB. Therefore, the designed antenna has better isolation of more than 20 dB.

Because of symmetry, the following S-parameters similarities are remarked:

$$\begin{aligned}
S_{11} &= S_{22} = S_{33} = S_{44} = S_{55} = S_{66}, \\
S_{21} &= S_{32} = S_{54} = S_{65}, \\
S_{31} &= S_{64}, \\
S_{41} &= S_{63}, \\
S_{51} &= S_{53} = S_{62} = S_{42}, \\
S_{61} &= S_{43}
\end{aligned} \tag{1}$$

4. Array Parameters

The performance of the proposed six-element antenna array is shown and discussed in this section.

4.1. S-Parameters

The simulated S-parameters for the proposed MIMO antenna are previously shown in Figure 7. Figure 8 illustrates the simulated and measured reflection coefficient of Ant 1.
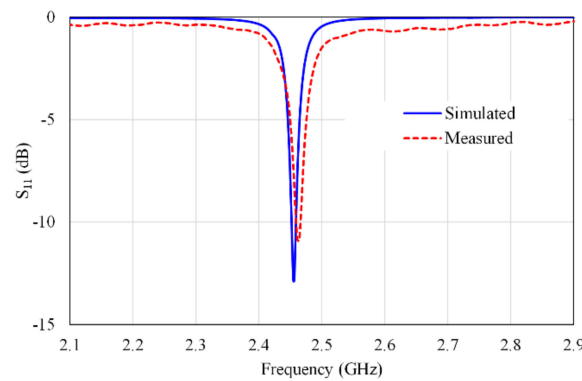

Figure 8. Simulated and measured S_{11}.

The reflection coefficients of other antennas (S_{22}, S_{33}, S_{44}, S_{55}, and S_{66}) are in close agreement with the results presented in Figure 8. Figure 9 shows the efficiency of the proposed MIMO antenna. It is observed from this figure, that the efficiencies of Ant 1, Ant 3, Ant 4, and Ant 6 are about 57–63%, however the efficiencies of Ant 2 and Ant 5 are about 62–65% in the operation bandwidth.
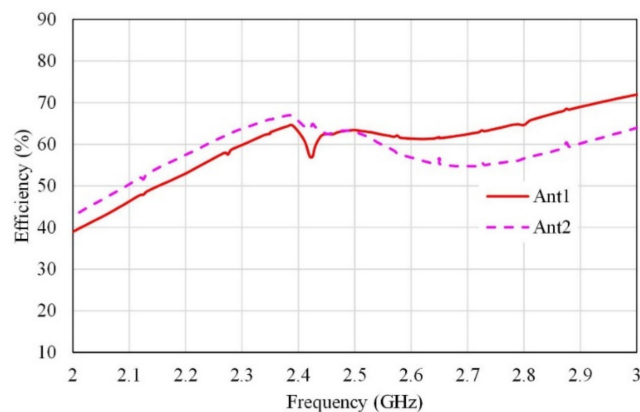

Figure 9. MIMO antenna radiation efficiency.

The simulated and measured isolations of these stated antennas (S_{21}, S_{31}, S_{41}, S_{51}, S_{61}, and S_{52}) are shown in Figure 10. Thus, high isolations between antennas are obtained, which are better than 20 dB overall.
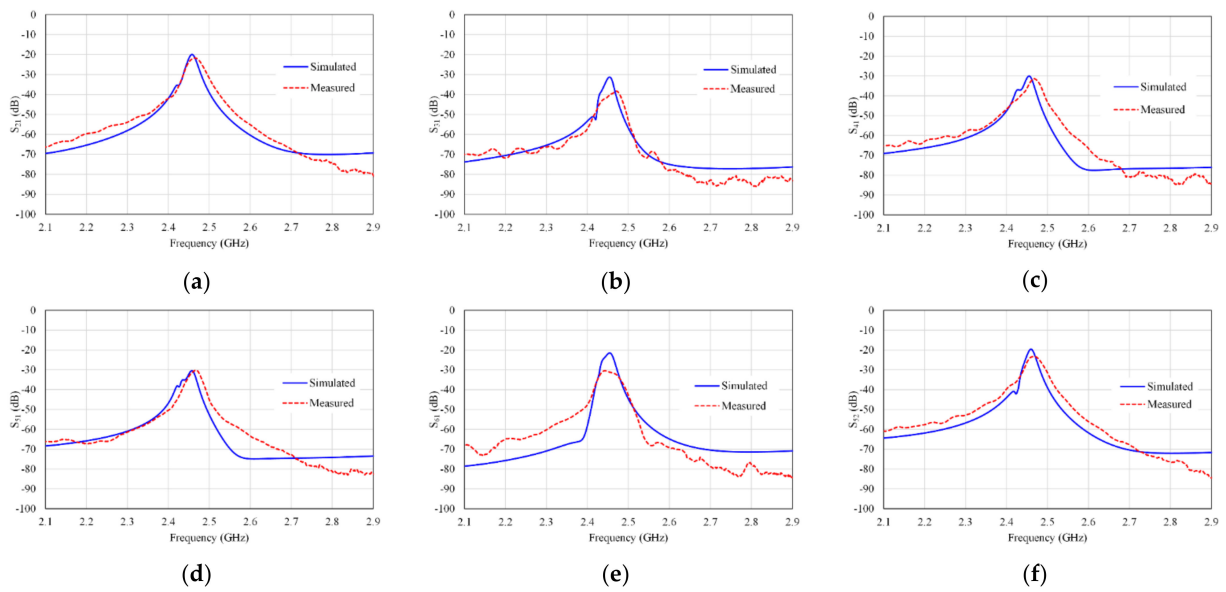
Figure 10. Simulated and measured S parameters (**a**) S_{21}, (**b**) S_{31}, (**c**) S_{41}, (**d**) S_{51}, (**e**) S_{61}, and (**f**) S_{52}.

4.2. Radiation Performances

The radiation patterns of the presented array antenna are analyzed and measured. Figures 11 and 12 show the simulated far-field radiation patterns of a six-port MIMO array.
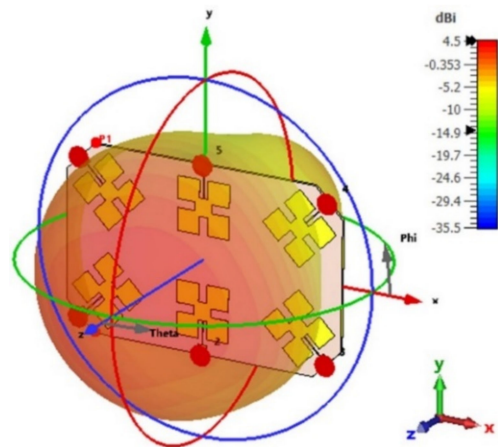

Figure 11. The simulated 3D radiation pattern of Ant 1, Ant 3, Ant 4, and Ant 6 at 2.45 GHz.
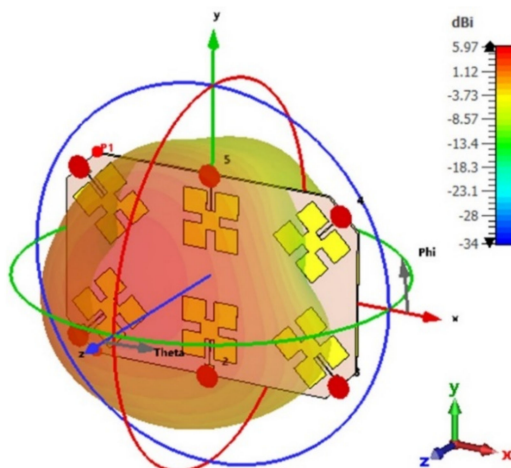

Figure 12. The simulated 3D radiation pattern of Ant 2, and Ant 5 at 2.45 GHz.

The gain of a single element is 4.21 dB as given in Figure 3 for the short ground plane. For the array, the gain becomes 4.5 dB for Ant 1, Ant 3, Ant 4, and Ant 6 (as given in Figure 11) and 5.97 dB for Ant 2 and Ant 5 (as given in Figure 12). This is expected since in the array configuration, the ground plane is large and most of the radiation comes from the front side.

Figure 13 shows the co- and cross-polarized radiation patterns for the suggested antenna at 2.45 GHz on the xz-plane, yz-plane, and xy-plane, respectively.
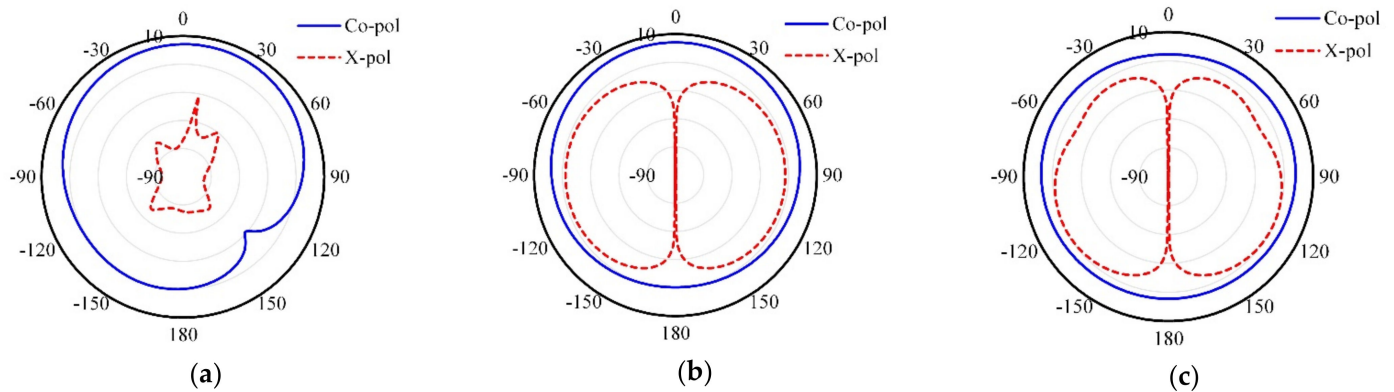

Figure 13. Co-polarized and cross-polarized radiation patterns of the proposed antenna (**a**) xz-plane, (**b**) yz-plane, and (**c**) xy-plane.

The normalized 2D radiation patterns for the fabricated prototype are measured and compared with the simulated ones, as shown in Figure 14.
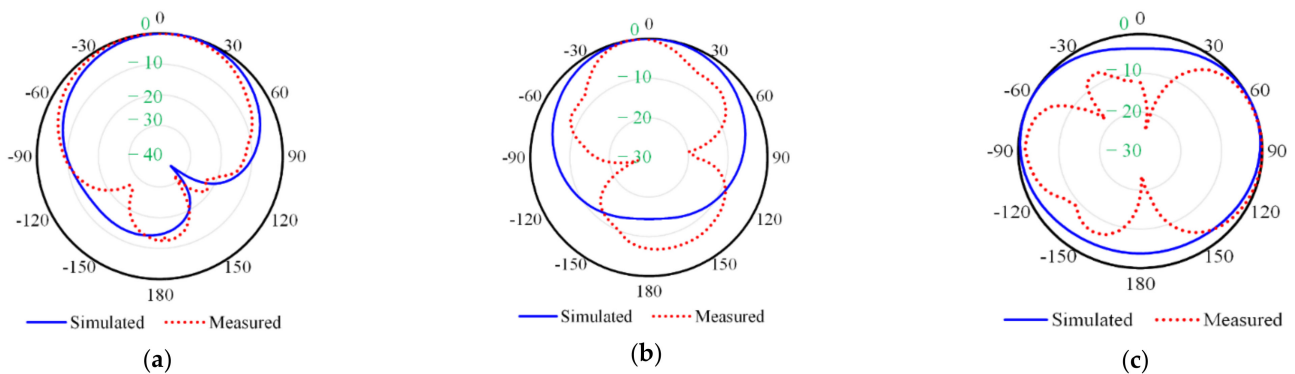
Figure 14. The simulated and measured radiation pattern of the proposed antenna at 2.45 GHz on the (**a**) xz-plane, (**b**) yz-plane, and (**c**) xy-plane.

Figure 14 shows the simulated and measured radiation patterns of the six-port MIMO antenna at 2.45 GHz on the xz-plane, yz-plane, and xy-plane, respectively.

To measure the radiation patterns for the proposed antenna, the antenna measurement system GEOZONDAS in a time domain (GEOZONDAS-TDAMS) is used [43]. A measurement setup was established to validate the far-field radiation pattern of the antenna. The antenna under test was placed on the top of the rotor.

The results in Figure 15 illustrate the co-polarized (co-pol) and cross-polarized (x-pol) radiation patterns for the proposed MIMO antenna in the xz-plane.

Figure 15. Radiation patterns of the proposed MIMO antenna in the xz-plane, (**a**) co-polarized and (**b**) cross-polarized.

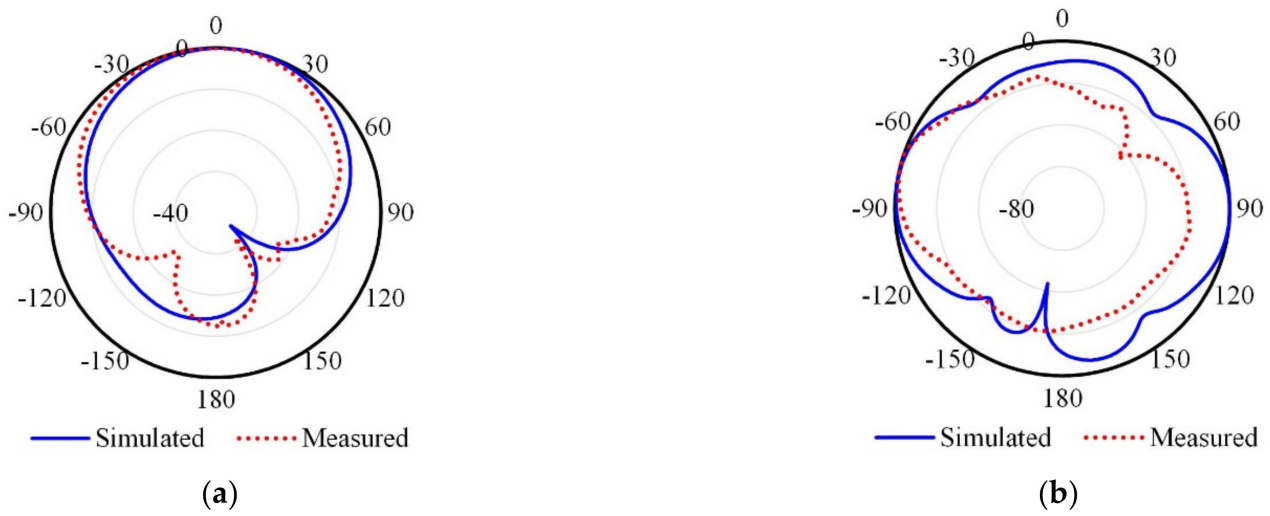## 5. MIMO Performance Parameters

To evaluate the potential MIMO performance of the proposed antenna array, the envelope correlation coefficient (ECC), the diversity gain (DG), the mean effective gain (MEG), and the channel capacity loss (CCL) are measured and analyzed.

The ECC parameter is used to measure the performance of the MIMO antenna system and it can be calculated using the S parameter method by the following equation [44,45]:

$$\rho_{ij} = \frac{\left|S_{ii}^{*}S_{ij} + S_{ji}^{*}S_{jj}\right|^{2}}{\left(1 - |S_{ii}|^{2} - S_{ij}^{2}\right)\left(1 - |S_{ji}|^{2} - S_{jj}^{2}\right)} \tag{2}$$

where $i = 1, 2, 3, 4, 5, 6$ and $j = i + 1, i + 2, \ldots, 6$. In our design, the 15 values of ECC are calculated, which are; $\rho_{12}, \rho_{13}, \rho_{14}, \rho_{15}, \rho_{16}, \rho_{23}, \rho_{24}, \rho_{25}, \rho_{26}, \rho_{34}, \rho_{35}, \rho_{36}, \rho_{45}, \rho_{46}$, and ρ_{56}. The spectral efficiency of the MIMO antenna system suffers when the ECC becomes high. It means that the lower value of ECC is preferable [9]. When the value of ρ approaches 0, a MIMO antenna system exhibits near-perfect performance [46].

In addition, the value of ECC can be calculated by using the radiation pattern method which is more accurate than the S parameter method. The ECC between Ant *i* and Ant *j* can be calculated using their far-field radiation patterns with the following equation [47,48]:

$$\rho_{ij} = \frac{\left|\int \int_{4\pi} \overline{F_i}(\theta, \varphi) \cdot \overline{F_j}^{*}(\theta, \varphi)d\Omega\right|^{2}}{\int \int_{4\pi} |\overline{F_i}(\theta, \varphi)|^{2}d\Omega \cdot \int \int_{4\pi} |\overline{F_j}(\theta, \varphi)|^{2}d\Omega} \tag{3}$$

Figure 16 displays the result of the ECC curves, which are calculated from both the S-parameter and the radiation pattern methods.

It is observed from this figure that the maximum values of ECC have occurred between Ant 1 and Ant 2 (ρ_{12}), Ant 2 and Ant 3 (ρ_{23}), Ant 4 and Ant 5 (ρ_{45}), and Ant 5 and Ant 6 (ρ_{56}). The maximum value of ECC is about 0.16.

An estimate of DG performance depends on measuring the transmission power loss with a value of it set to 10 dB [49,50]. The DG can be computed by:

$$DG_{ij} = 10 \sqrt{1 - |\rho_{ij}|^{2}} \tag{4}$$

Figure 17 shows the DG curves of our array, which are near 10 dB in the operation bandwidth. It means the proposed MIMO antenna has a good diversity performance.
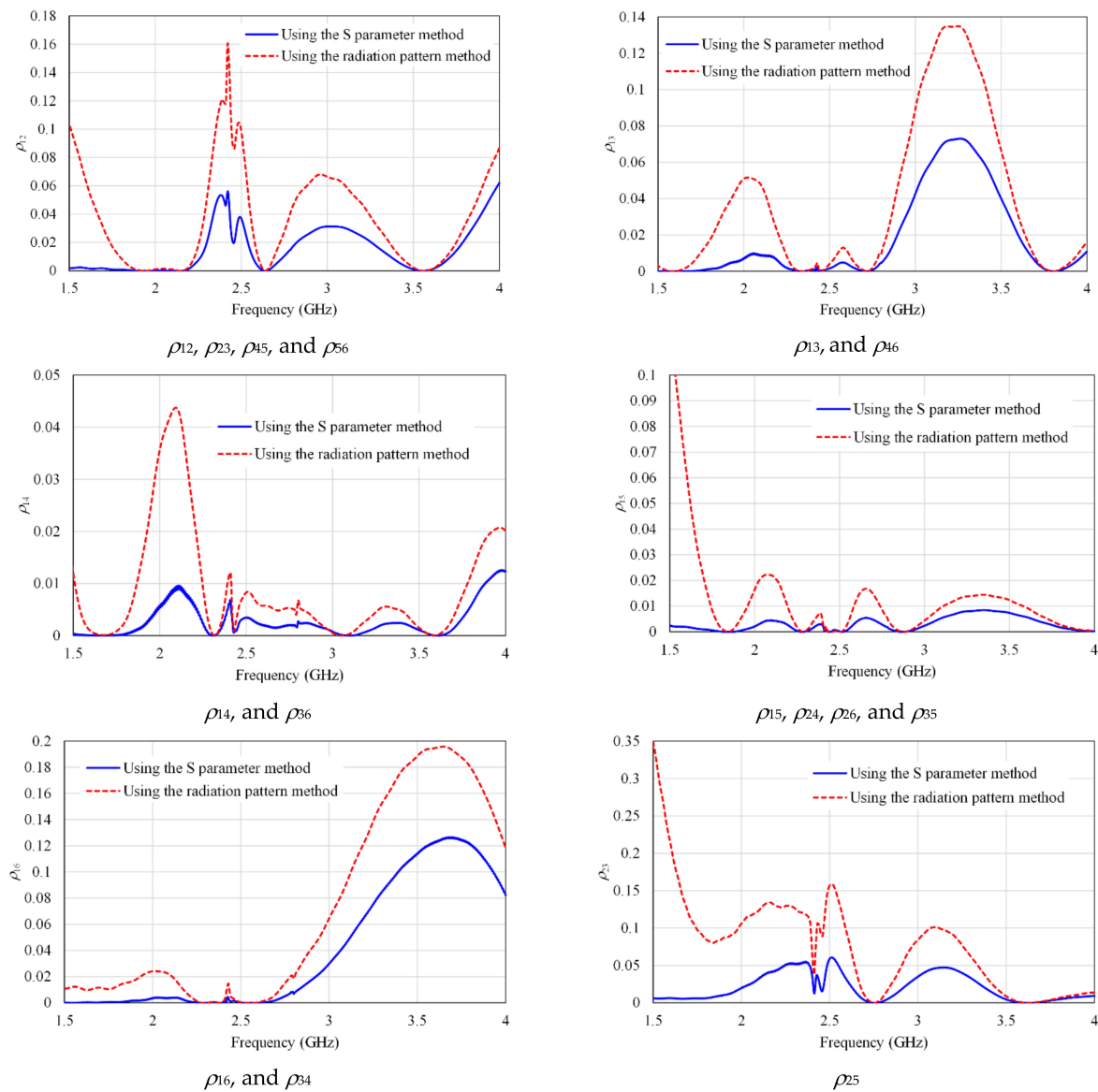
$\rho_{12}, \rho_{23}, \rho_{45},$ and ρ_{56}

$\rho_{13},$ and ρ_{46}

$\rho_{14},$ and ρ_{36}

$\rho_{15}, \rho_{24}, \rho_{26},$ and ρ_{35}

$\rho_{16},$ and ρ_{34}

ρ_{25}

Figure 16. The ECC of the proposed MIMO antenna using the S parameter and radiation pattern methods.

The MEG is another essential parameter used to measure the diversity performance of the MIMO antenna. It is the ratio between the mean powers received by diversity gain to the mean power received by an isotropic antenna. The MEG can be measured using the following equation [51,52]:

$$\text{MEG}_i = 0.5\eta_{iRad} = 0.5\left(1 - \sum_{j=1}^{6}|S_{ij}|^2\right) \tag{5}$$

where i is the active gain and η_{iRad} is the radiation efficiency of this antenna. In our design, two-MEG curves are calculated from the S-parameters, as shown in Figure 18. The first one (MEG1) is when Ant 1, Ant 3, Ant 4, or Ant 6 is under observation, however, the second curve (MEG2) is when Ant 2 or Ant 5 is under observation.

DG$_{12}$, DG$_{23}$, DG$_{45}$, and DG$_{56}$

DG$_{13}$, and DG$_{46}$

DG$_{14}$, and DG$_{36}$

DG$_{15}$, DG$_{24}$, DG$_{26}$, and DG$_{35}$

DG$_{16}$, and DG$_{34}$

DG$_{25}$

Figure 17. The DG of the proposed MIMO antenna by using the S parameter and radiation pattern methods.

Figure 18. The MEG of the proposed MIMO antenna. (MEG1) is when Ant 1, Ant 3, Ant 4, or Ant 6 is under observation, however, the second curve (MEG2) is when Ant 2 or Ant 5 is under observation.
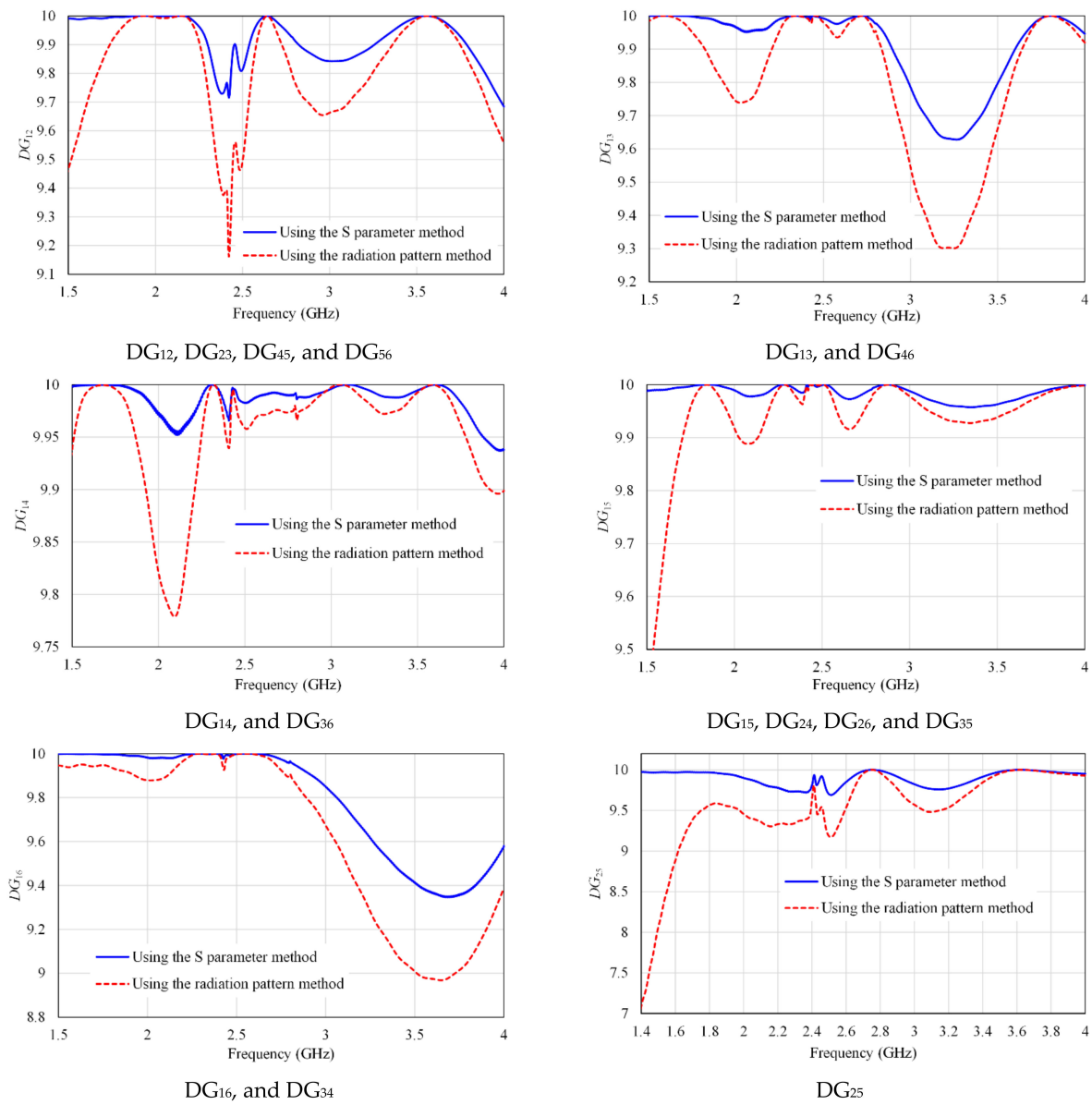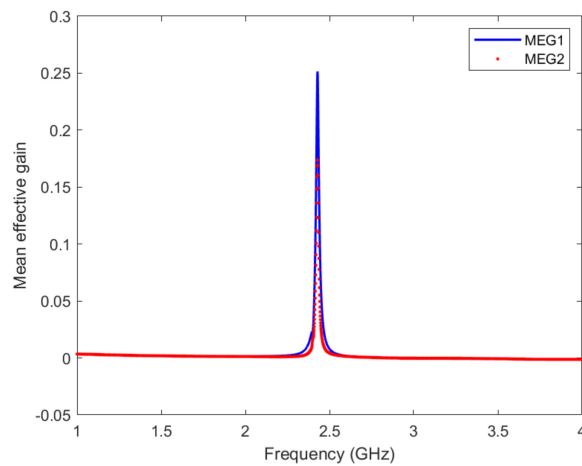
It is observed from this figure that the maximum values of MEGs have occurred when Ant 1, Ant 3, Ant 4, or Ant 6 is under observation. The maximum value of MEG is about 0.25.

The CCL of the MIMO antenna is also one of the most important parameters to measure diversity performance. It is used to define the maximum achievable limit of the information transmission rate, and it can be calculated using [46]:

$$CCL = -\log_2 \det(\alpha) \tag{6}$$

where

$$\alpha = \begin{bmatrix} \alpha_{12} & \alpha_{13} & \alpha_{14} & \alpha_{14} & \alpha_{15} & \alpha_{16} \\ \alpha_{21} & \alpha_{22} & \alpha_{23} & \alpha_{24} & \alpha_{25} & \alpha_{26} \\ \alpha_{31} & \alpha_{32} & \alpha_{33} & \alpha_{34} & \alpha_{35} & \alpha_{36} \\ \alpha_{41} & \alpha_{42} & \alpha_{43} & \alpha_{44} & \alpha_{45} & \alpha_{46} \\ \alpha_{51} & \alpha_{52} & \alpha_{53} & \alpha_{54} & \alpha_{55} & \alpha_{56} \\ \alpha_{61} & \alpha_{62} & \alpha_{63} & \alpha_{64} & \alpha_{65} & \alpha_{66} \end{bmatrix} \tag{7}$$

and

$$\alpha_{ii} = 1 - \sum_{j=1}^{6} |S_{ij}|^2 \tag{8}$$

$$ff_{ij} = -\left(S_{ii}^* S_{ij} + S_{ji}^* S_{jj} \right) \tag{9}$$

The computed values of CCL for the proposed antenna are shown in Figure 19. It is observed that the CCL is almost below the standard value of 0.4 bits/s/Hz for a practical MIMO antenna system in the operation bandwidth.
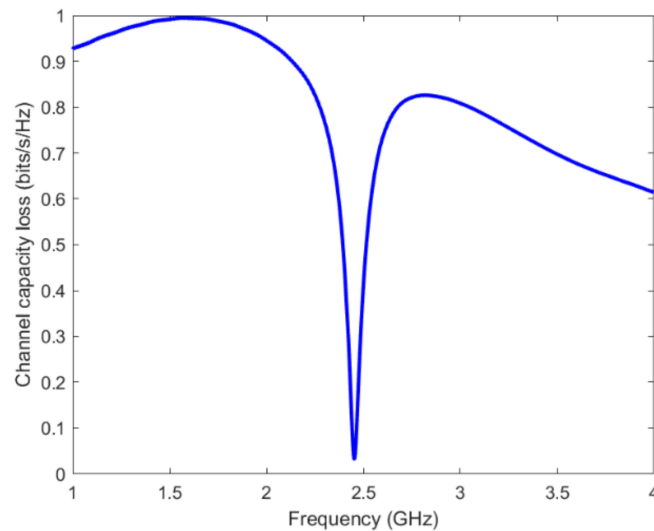

Figure 19. The CCL of the proposed MIMO antenna.

Then, we use our antenna parameters to show how the antenna mutual coupling affects the performance of transmission over a MIMO channel. For the DG estimation, the communication system is set to have a transmitter of one element, while the receiver has a six-elements array. QPSK modulation is conducted over a 1×6 quasi-static frequency-flat Rayleigh channel [53–55]. The simulation is conducted using MATLAB, and the channel path correlation and element coupling are taken into consideration. The suggested communication system operates at 2.45 GHz and the simulated SNR range is 0 to 15 dB.

Figure 20 shows the BER achieved using diversity gain with and without consideration of element coupling. The results are also compared to BER for no diversity gain. As observed from this figure that the diversity gain when BER is equal to 0.01 is about 12 dB.
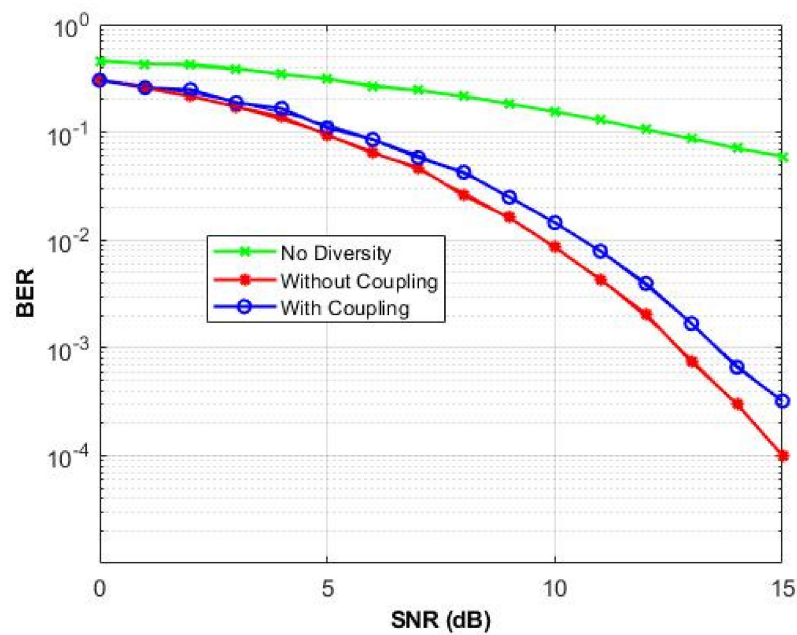
Figure 20. The BER vs. SNR curve.

To investigate MIMO channel capacity, a simulation is conducted to investigate beam steering to six users, using the six-element proposed array. The spectral efficiency of the MIMO system compared to the SISO system is shown in Figure 21.
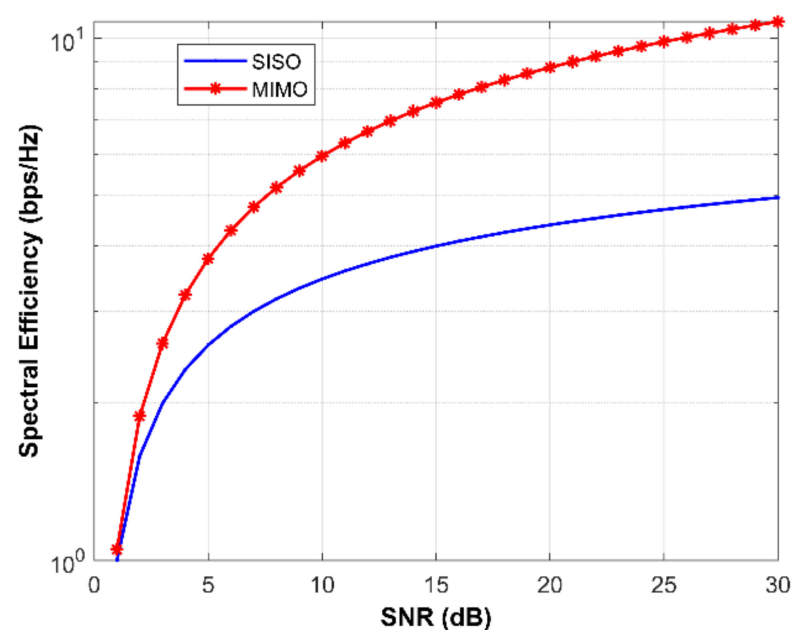
Figure 21. The channel capacity of the proposed MIMO antenna.

Table 1 compares the proposed design with some recently reported 5G terminal MIMO arrays. The table shows how good isolation is achieved in the proposed work. Compared to the recent work, the proposed design shows wider operating bandwidth with very good isolations. In addition, the ECC value is better which makes this design more appropriate in terms of performance and isolation, thus making it highly recommended for IoT mobile applications.

Table 1 shows how the implementation of our suggested structure has the best performance although the six elements are arranged in a compact size with coupling between the antenna array elements <-20 dB.

Table 1. Comparison performance.

Ref.	Bandwidth (GHz)	Isolation Level (dB)	ECC Value	Size ($\lambda_0 \times \lambda_0$)	Number of Radiating Elements
[13]	24.1–27.2	16	0.1	2.08 × 1.73	2
[14]	3.4–3.6	15	0.16	1.43 × 0.85	4
[16]	3.4–3.6	18.4	0.08	1.2 × 1.2	8
[21]	3.4–3.6	20	0.06	1.75 × 0.88	4
[22]	3.4–3.6	13	0.1	1.63 × 0.82	8
[23]	3.6–9.8	17.3	0.04	1.06 × 0.75	4
[24]	2–3	8	0.25	0.57 × 0.57	2
This Work	2.43–2.48	20	0.01	1.22 × 0.79	6

6. Beamforming Function

After developing the MIMO array and testing the antenna parameters, we try to achieve the beamforming functions. Figure 22 shows the block diagram of the modeling of the receiver with beamforming. The simulation is conducted using a SIMULINK environment. The signal transmitter implements a QAM modulator and passes a raised cosine transmit filter. The channel uses the additive white Gaussian noise (AWGN) channel. The receiver is narrowband plane waves incident on the elements of the sensor array.
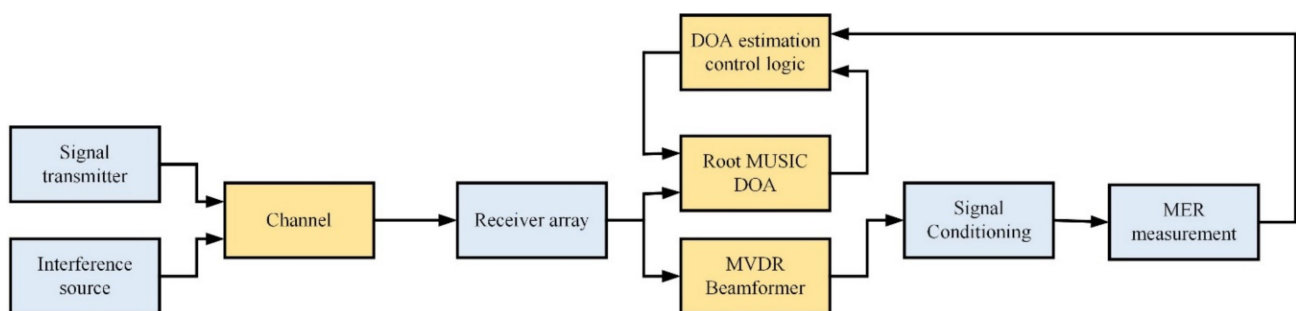

Figure 22. Modeling of Beamforming Receiver.

We use an adaptive beamforming system to suppress the interference signal and thus enhance the SINR. The beamformer depends on implementing the narrowband minimum-variance distortionless response (MVDR) [56]. The beamformer preserves the signal power in the given direction while suppressing interferences from other directions. The system depends on estimating the direction of arrival (DOA) of various signals to localize the direction of desired and interference signals. In particular, we used high-resolution DOA estimation based on the root-MUSIC DOA that is based on the eigenvalue decomposition of the covariance matrix of the receiver sensor array. After identifying the directions of interference and transmitted signals, we use MVDR beamforming to suppress the interference and enhance the desired signal. In addition, adaptive negative feedback EVM is used to accurately follow DOA for both the wanted signal source and the unwanted interference [56].

The model assumes receiving data from D uncorrelated or signal sources $s_d(t)$. In addition, for an array with M elements, the mth element data $x_m(t)$ includes AWGN $n_m(t)$. We thus have:

$$x(t) = As(t) + n(t) \tag{10}$$

$$s(t) = [s_1(t), s_2(t), \ldots, s_M(t)] \tag{11}$$

$$A = [a(\theta_1)|a(\theta_2)|\ldots|a(\theta_D)] \tag{12}$$

where $x(t)$ is an $M \times 1$ vector of a received signal at time t.

The $M \times D$ matrix A represents the arrival vectors, where each source contributes to one column of A. θ_d represents azimuth and the elevation angles of the dth source. $S(t)$ is a D-by-1 vector of source signal values from D sources.

The covariance matrix, R_x, is derived from the received signal data and is associated with the signal covariance matrix R_s and the noise covariance matrix.

$$R_x = E\left\{ xx^H \right\} = AR_s A^H + \sigma_n^2 I \tag{13}$$

$$R_s = E\left\{ ss^H \right\} \tag{14}$$

Multiple measurements of the sensor data are averaged to obtain R_x

$$R_x = \frac{1}{T} \sum_{k=1}^{T} x(t)x(t)^H \tag{15}$$

where T is the number of snapshots.

The estimation of the DOA is enhanced through a control logic that makes use of the error vector magnitude (EVM) that is computed from the modulation error ratio (MER).

Three cases are studied in this work which are: case 1: (3×2) array with signal angles (azimuthal, elevation) $(45°, 45°)$ and interference angles (azimuthal, elevation) $(30°, 90°)$; case 2: (3×2) antenna array with signal angles $(30°, 45°)$ and interference angles $(45°, 70°)$, and case 3: (3×4) array using two (3×2) arrays, with signal angles $(30°, 45°)$ and interference angles $(45°, 70°)$, respectively.

The eight-PSK I/Q amplitude constellation diagrams for case 1, case 2, and case 3 are shown in Figure 23a–c, respectively. The signal and interference input spectrum of the RF transmitter, with a peak power of -20 dBm is shown in Figure 24.
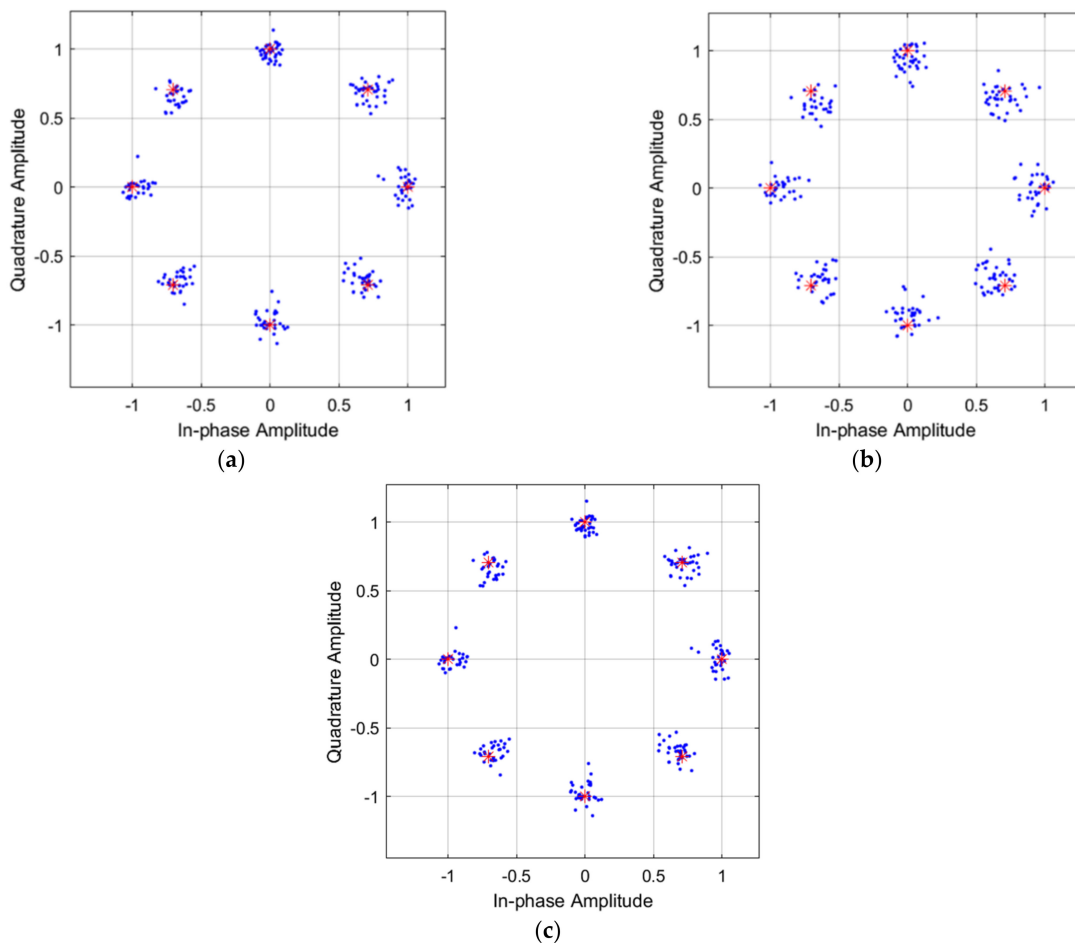

Figure 23. The constellation diagrams of 8 PSK for (**a**) case 1, (**b**) case 2, and (**c**) case 3.
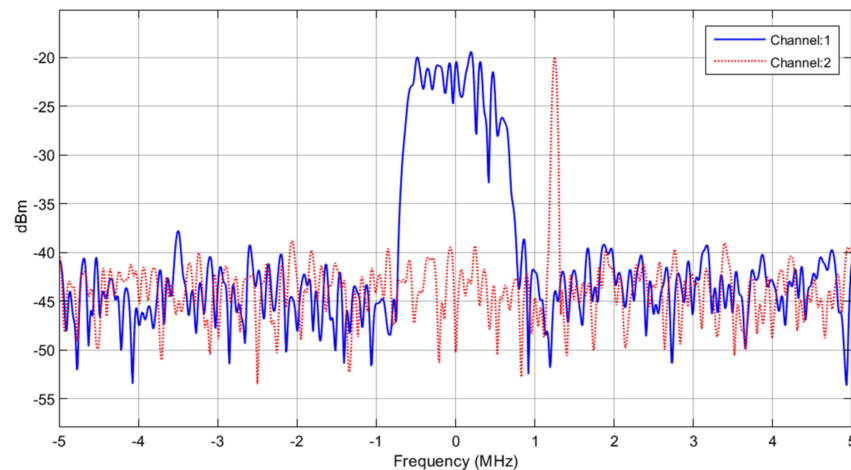
Figure 24. Signal (channel 1) and interference (channel 2) input spectrum of the RF transmitter.

The signal and interference input spectrum of the RF receiver, without beamforming and with beamforming, case 1, case 2, and case 3, are shown in Figures 25–27, respectively.
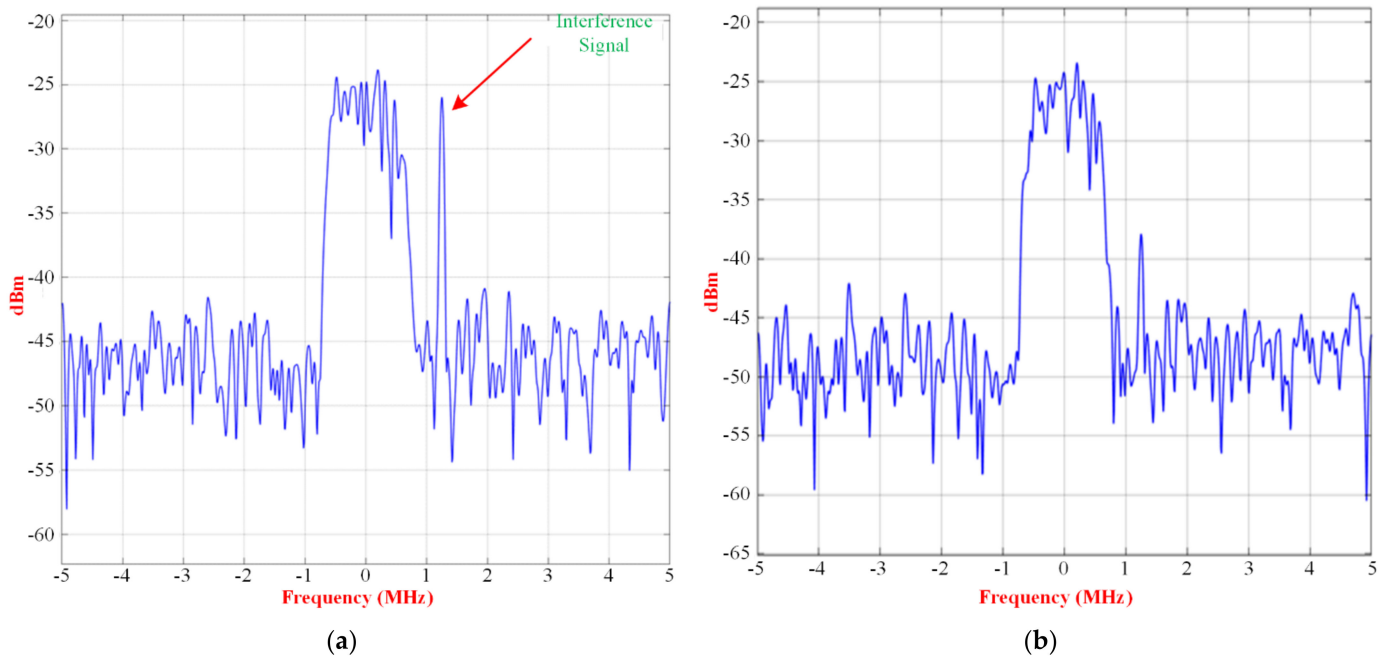

(a)

(b)

Figure 25. Signal and interference input spectrum of the RF receiver for case 1 (**a**) without beamforming, and after (**b**) with beamforming.

There is an improvement of 12 dB of peak power in the interference with the use of beamforming for case 1. For case 2, the interference and signals, which have similar peak power, are close and little interference suppression can be achieved by the beamformer.

However, for the same direction of arrivals, a better resolution is achieved with an array size of 3 × 4 in case 3, and the interference signal is almost removed, compared to the desired signal. However, for the same direction of arrivals, better resolution is achieved with an array size of 3 × 4 in case 3, and the interference signal is almost removed, compared to the desired signal.
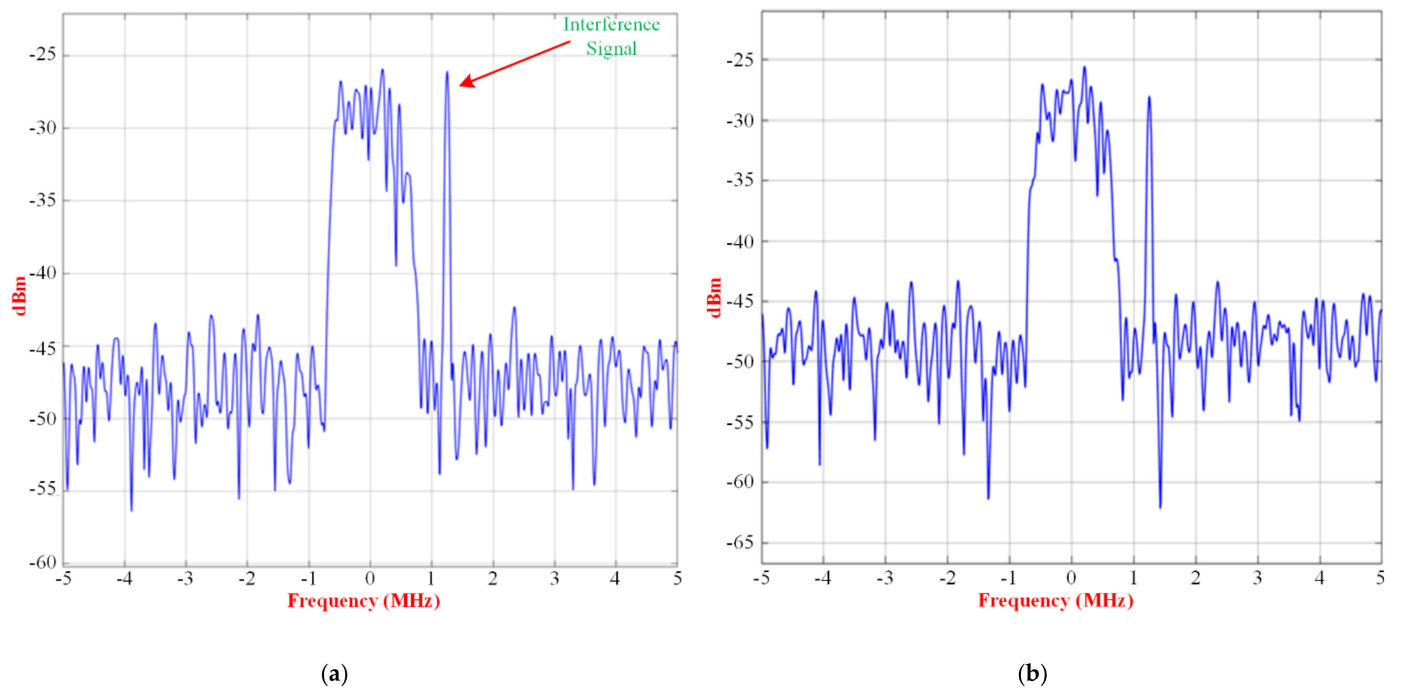
Figure 26. Signal and interference input spectrum of the RF receiver for case 2 (**a**) without beamforming, and (**b**) with beamforming.
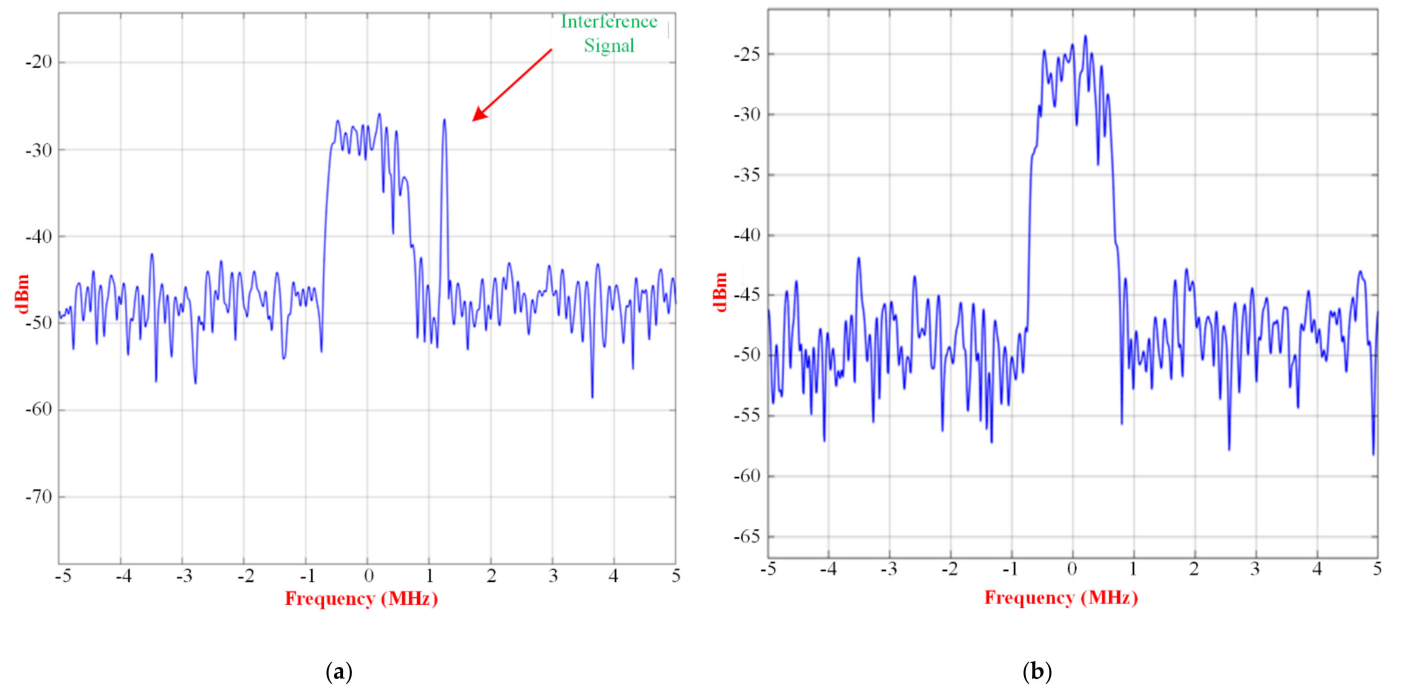
Figure 27. Signal and interference input spectrum of the RF receiver for case 3 (**a**) without beamforming, and (**b**) with beamforming.

Figure 28a shows no effect of interference on signal for case 1, as described by the difference between the steered beams to the signal and interference directions. However, when the interference angles are changed to (45°, 70°) and the signal angles are changed to (30°, 45°) (case 2), the beam level of interference becomes larger compared to case 1, and the difference between the interference and signal levels becomes small, as shown in Figure 28b.

(**a**)

(**b**)

(**c**)
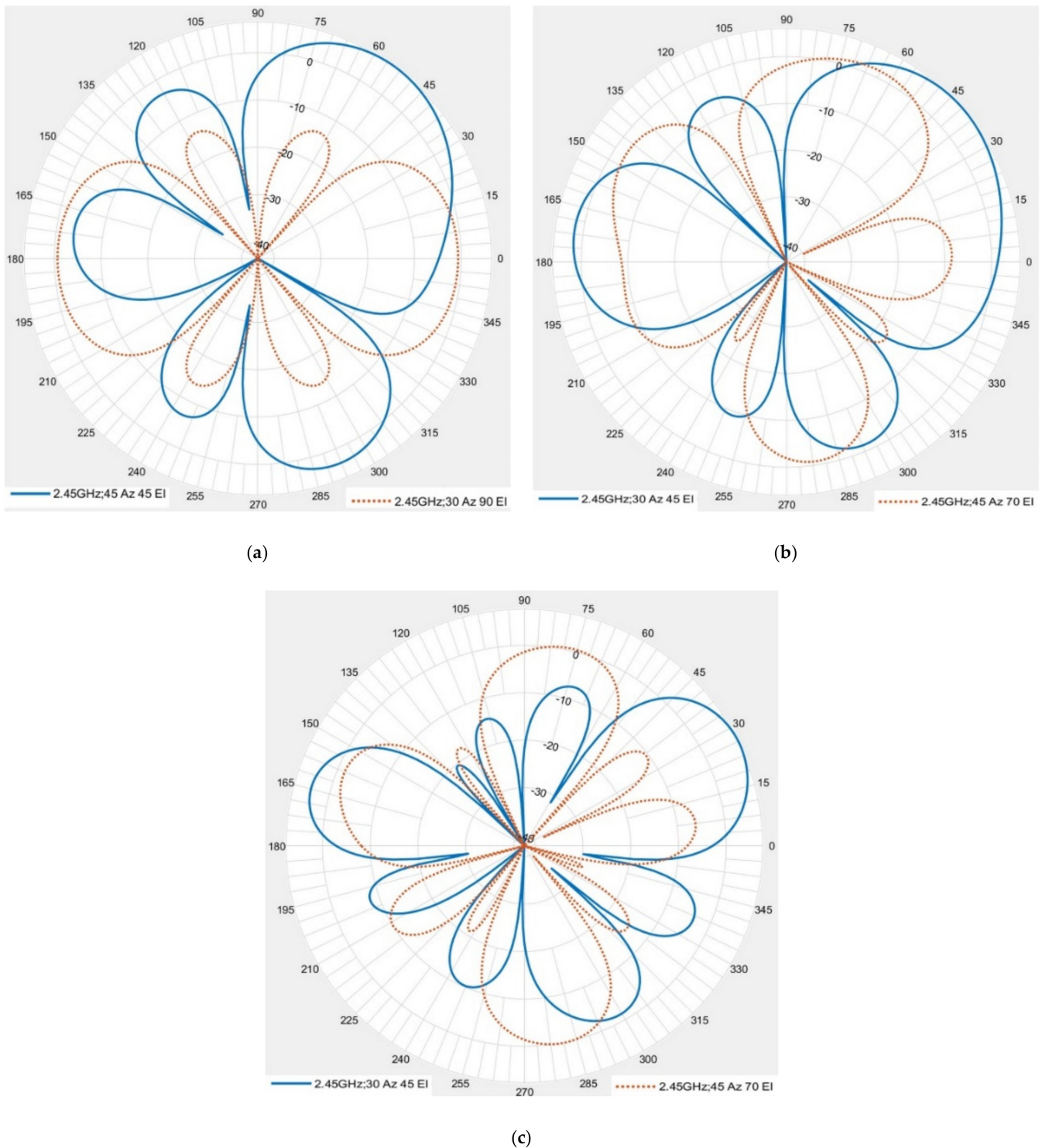
Figure 28. Signal and interference beam-steering for (**a**) case 1 (**b**) case 2 (**c**) case 3.

To solve this problem, the number of antenna arrays is increased to 4×3 (case 3). Figure 28c shows that no effect of the interference on the signal for the interference angles ($45°$, $70°$) and the signal angles ($30°$, $45°$).

The relationship between error vector magnitude (EVM) and signal-to-noise ratio (SNR) is shown in Figure 29. The EVM for case 2 is greater than the other cases by around 22 at -10 dB SNR. This difference reduces exponentially to reach zero at 12 dB SNR. Table 2 summarizes the performance for those three cases.

Figure 29. EVM versus SNR over AWGN channels.

Table 2. The performance for the three cases.

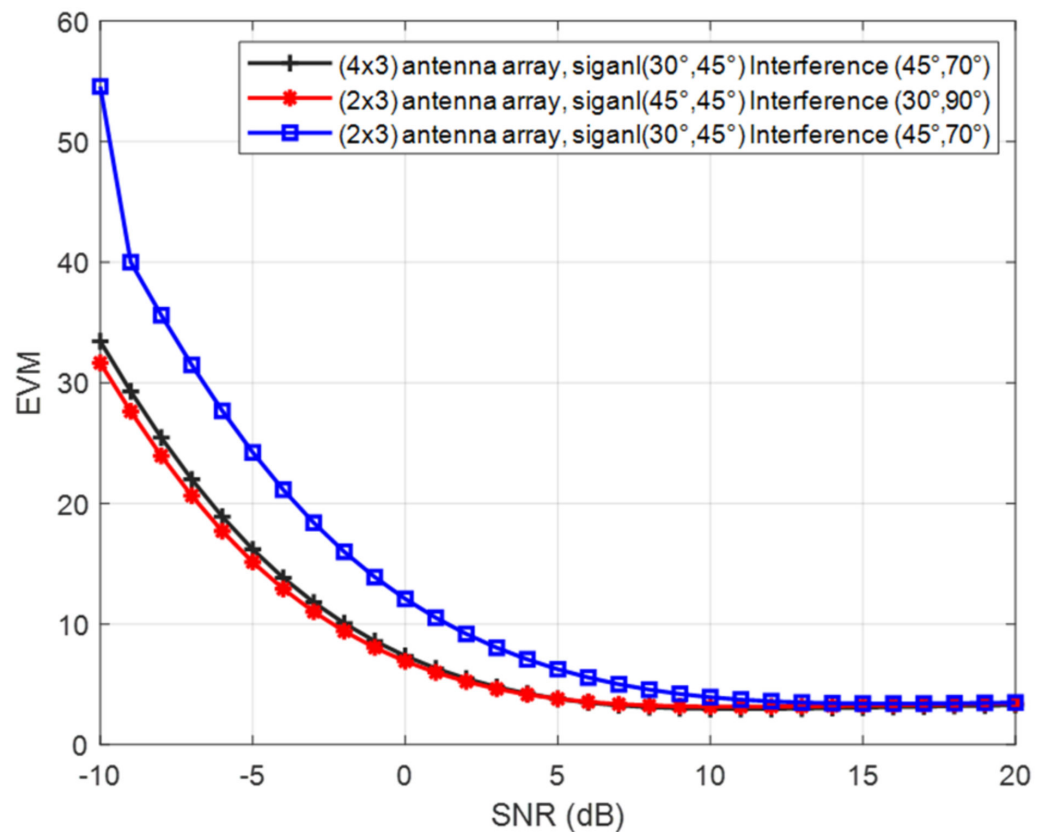| Case Number	Signal (Azimuthal, Elevation) Angles	Interference (Azimuthal, Elevation) Angles	Array Size	Interference Peak Power without Beamforming in dBm	Interference Peak Power with Beamforming in dBm
1	(45°, 45°)	(30°, 90°)	3 × 2	−26	−38
2	(30°, 45°)	(45°, 70°)	3 × 2	−26	−28
3	(30°, 45°)	(45°, 70°)	3 × 4	−27	Almost removed

7. Performance in Regional Area Network

The analysis is conducted assuming various schemes with particular channel models and channel coding. In particular, five communication schemes are assumed. The first three schemes assume an additive white Gaussian noise (AWGN) channel with the use of convolution coding with a code rate of 1/2 and soft decoding (1), block coding with a code rate of 3/7 and soft decoding (2); and no channel coding (3). Scheme four assumes a Rician channel with K = 10 dB and a diversity order of 6 and scheme five assumes a Rayleigh fading channel with a diversity order of 6. Using the bit error tool of Matlab, the required bit SNR for an error rate of around 10^{-5} is found to be approximately 4.1, 6.8, 9.5, 10.2, and 13.5 dB for modes 1 to 5, respectively [57,58]. The transmitted power signal, as well as the interference signal, are assumed to be of −10 dBm level each.

The signal source is assumed to be located at a distance ranging from 10 to 100 km, while the interference level is assumed to be at a much shorter distance of 1 km. For each of the five assumed communication systems schemes, simulations are conducted first using beamforming to suppress the interference signal and then without the use of beamforming. Figure 30 shows the estimated data rate versus the coverage distance. The figure illustrates the importance of beamforming in enhancing the data rate by a ratio of 100.
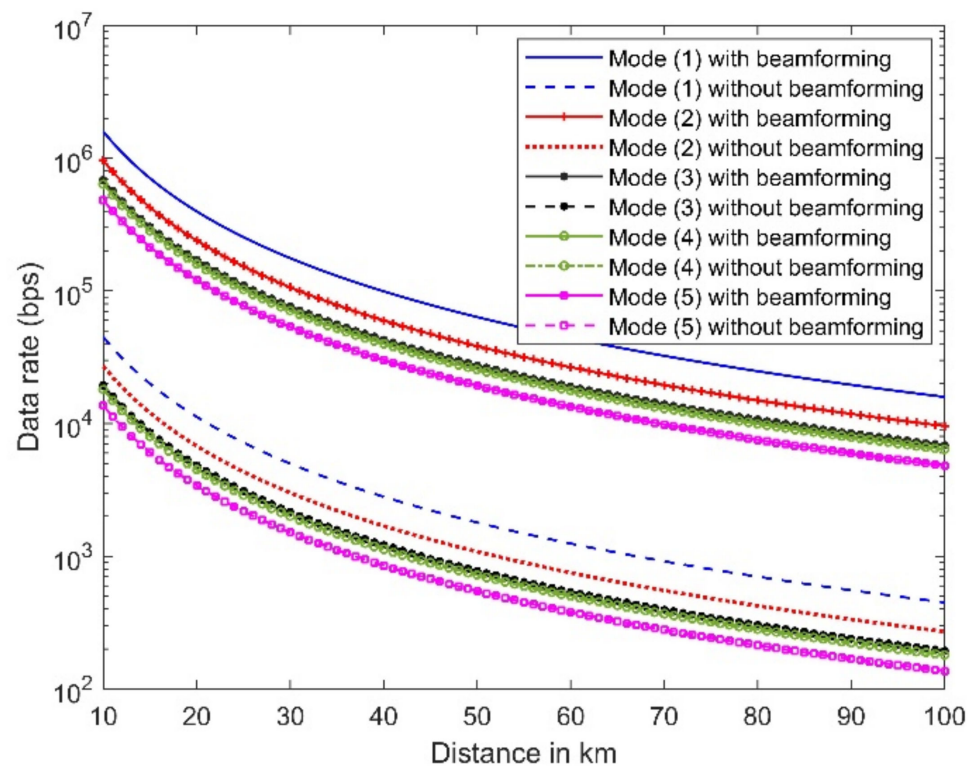
Figure 30. The estimated data rate versus distance corresponds to five communication scheme modes with and without the use of beamforming.

8. Conclusions

A system is proposed for extended coverage of the regional area networks. The system depends on a new compact 3×2 array module at 2.45 GHz. Array elements have acceptable isolation of (≤ -20 dB) and ECC is less than 0.2 for any two elements. One or more of these modules can be used to enhance in a central node of the system to collect with other nodes and make use of the array to enhance the signal and reduce unwanted interference levels.

The simulation results illustrate the potential of such a system in providing data rates of acceptable levels for IoT applications for extended coverage networks. Such a system is useful in collecting data in desert areas from widely spaced sensor units. The extended coverage also allows for the connection of the system to a node with cellular coverage to send data through the internet to monitor and control centers. The application examples include collecting environmental data from weather stations and tree-health assessments of palm tree farms.

Author Contributions: Conceptualization, W.M.A. and A.-F.A.S.; methodology, W.M.A., A.-F.A.S., I.E. and M.A.A.; software, W.M.A.; validation, W.M.A.; formal analysis, W.M.A., A.-F.A.S., I.E. and M.A.A.; investigation, A.-F.A.S. and I.E.; resources, A.-F.A.S. and I.E.; data curation, W.M.A.; writing—original draft preparation, W.M.A.; writing—review and editing, W.M.A., A.-F.A.S., I.E. and M.A.A.; visualization, W.M.A. and A.-F.A.S.; supervision, A.-F.A.S. and I.E.; project administration, A.-F.A.S.; funding acquisition, A.-F.A.S. All authors have read and agreed to the published version of the manuscript.

Institutional Review Board Statement: Not applicable.

Informed Consent Statement: Not applicable.

Data Availability Statement: Not applicable.

Conflicts of Interest: The authors declare no conflict of interest.

References

1. Kumar, P.; Urooj, S.; Malibari, A. Design and implementation of quad-element super-wideband MIMO antenna for IoT applications. *IEEE Access* **2020**, *8*, 226697–226704. [CrossRef]
2. Romputtal, A.; Phongcharoenpanich, C. IoT-linked integrated NFC and dual band UHF/2.45 GHz RFID reader antenna scheme. *IEEE Access* **2019**, *7*, 177832–177843. [CrossRef]
3. Kirtania, S.G.; Younes, B.A.; Hossain, A.R.; Karacolak, T.; Sekhar, P.K. CPW-fed flexible ultra-wideband antenna for IoT applications. *Micromachines* **2021**, *12*, 453. [CrossRef]
4. Al-Gburi, A.J.A.; Zakaria, Z.; Palandoken, M.; Ibrahim, I.M.; Althuwayb, A.; Ahmad, S.; Al-Bawri, S.S. Super Compact UWB Monopole Antenna for Small IoT Devices. *Comput. Mater. Contin.* **2022**, *73*, 2785–2799.
5. Sabban, A. Wearable Circular Polarized Antennas for Health Care, 5G, Energy Harvesting, and IoT Systems. *Electronics* **2022**, *11*, 427. [CrossRef]
6. Abdulkawi, W.M.; Nizam-Uddin, N.; Sheta, A.F.A.; Elshafiey, I.; Al-Shaalan, A.M. Towards an Efficient Chipless RFID System for Modern Applications in IoT Networks. *Appl. Sci.* **2021**, *11*, 8948. [CrossRef]
7. Thiruvenkadam, S.; Parthasarathy, E.; Palaniswamy, S.K.; Kumar, S.; Wang, L. Design and Performance Analysis of a Compact Planar MIMO Antenna for IoT Applications. *Sensors* **2021**, *21*, 7909. [CrossRef]
8. Ikram, M. 5G/B5G Internet of Things MIMO Antenna Design. *Signals* **2022**, *3*, 3. [CrossRef]
9. Abdulkawi, W.M.; Malik, W.A.; Rehman, S.U.; Aziz, A.; Sheta, A.F.A.; Alkanhal, M.A. Design of a Compact Dual-Band MIMO Antenna System with High-Diversity Gain Performance in Both Frequency Bands. *Micromachines* **2021**, *12*, 383. [CrossRef]
10. Al Abbas, E.; Ikram, M.; Mobashsher, A.T.; Abbosh, A. MIMO antenna system for multi-band millimeter-wave 5G and wideband 4G mobile communications. *IEEE Access* **2019**, *7*, 181916–181923. [CrossRef]
11. Abdullah, M.; Altaf, A.; Anjum, M.R.; Arain, Z.A.; Jamali, A.A.; Alibakhshikenari, M.; Falcone, F.; Limiti, E. Future smartphone: MIMO antenna system for 5G mobile terminals. *IEEE Access* **2021**, *9*, 91593–91603. [CrossRef]
12. Getu, B.N.; Andersen, J.B. The MIMO cube-a compact MIMO antenna. *IEEE Trans. Wirel. Commun.* **2005**, *4*, 1136–1141. [CrossRef]
13. Kiani, S.H.; Altaf, A.; Abdullah, M.; Muhammad, F.; Shoaib, N.; Anjum, M.R.; Damaševičius, R.; Blažauskas, T. Eight element side edged framed MIMO antenna array for future 5G smart phones. *Micromachines* **2020**, *11*, 956. [CrossRef] [PubMed]
14. Sarkar, D.; Saurav, K.; Srivastava, K.V. Dual band complementary split-ring resonator-loaded printed dipole antenna arrays for pattern diversity multiple-input–multiple-output applications. *IET Microw. Antennas Propag.* **2016**, *10*, 1113–1123. [CrossRef]
15. Li, Q.; Cheung, S.; Wu, D.; Yuk, T. Optically transparent dual-band MIMO antenna using micro-metal mesh conductive film for WLAN system. *IEEE Antennas Wirel. Propag. Lett.* **2016**, *16*, 920–923. [CrossRef]
16. Kabiri, Y.; Borja, A.L.; Kelly, J.R.; Xiao, P. A technique for MIMO antenna design with flexible element number and pattern diversity. *IEEE Access* **2019**, *7*, 86157–86167. [CrossRef]
17. Desai, A.; Bui, C.D.; Patel, J.; Upadhyaya, T.; Byun, G.; Nguyen, T.K. Compact wideband four element optically transparent MIMO antenna for mm-wave 5G applications. *IEEE Access* **2020**, *8*, 194206–194217. [CrossRef]
18. Jiang, W.; Liu, B.; Cui, Y.; Hu, W. High-isolation eight-element MIMO array for 5G smartphone applications. *IEEE Access* **2019**, *7*, 34104–34112. [CrossRef]
19. Chen, X.; Zhang, S.; Li, Q. A review of mutual coupling in MIMO systems. *IEEE Access* **2018**, *6*, 24706–24719. [CrossRef]
20. Boukarkar, A.; Lin, X.Q.; Jiang, Y.; Nie, L.Y.; Mei, P.; Yu, Y.Q. A miniaturized extremely close-spaced four-element dual-band MIMO antenna system with polarization and pattern diversity. *IEEE Antennas Wirel. Propag. Lett.* **2017**, *17*, 134–137. [CrossRef]
21. Sun, L.; Feng, H.; Li, Y.; Zhang, Z. Compact 5G MIMO mobile phone antennas with tightly arranged orthogonal-mode pairs. *IEEE Trans. Antennas Propag.* **2018**, *66*, 6364–6369. [CrossRef]
22. Li, J.; Zhang, X.; Wang, Z.; Chen, X.; Chen, J.; Li, Y.; Zhang, A. Dual-band eight-antenna array design for MIMO applications in 5G mobile terminals. *IEEE Access* **2019**, *7*, 71636–71644. [CrossRef]
23. Tiwari, R.; Singh, P.; Kanaujia, B.; Srivastava, K. Neutralization Technique Based Two and Four Port High Isolation MIMO Antennas for UWB Communication. *AEU—Int. J. Electron. Commun.* **2019**, *110*, 152828. [CrossRef]
24. Shen, X.; Liu, F.; Zhao, L.; Huang, G.-L.; Shi, X.; Huang, Q.; Chen, A. Decoupling of Two Strongly Coupled Dual-Band Antennas With Reactively Loaded Dummy Element Array. *IEEE Access* **2019**, *7*, 154672–154682. [CrossRef]
25. Ren, Z.; Zhao, A. Dual-Band MIMO Antenna with Compact Self-Decoupled Antenna Pairs for 5G Mobile Applications. *IEEE Access* **2019**, *7*, 82288–82296. [CrossRef]
26. Hu, W.; Qian, L.; Gao, S.; Wen, L.-H.; Luo, Q.; Xu, H.; Liu, X.-K.; Liu, Y.; Wang, W. Dual-Band Eight-Element MIMO Array Using Multi-Slot Decoupling Technique for 5G Terminals. *IEEE Access* **2019**, *7*, 153910–153920. [CrossRef]
27. Abdullah, M.; Kiani, S.; Iqbal, A. Eight Element Multiple-Input Multiple-Output (MIMO) Antenna for 5G Mobile Applications. *IEEE Access* **2019**, *7*, 134488–134495. [CrossRef]
28. Li, T.; Geyi, W. Design of MIMO beamforming antenna array for mobile handsets. *Prog. Electromagn. Res. C* **2019**, *94*, 13–28. [CrossRef]
29. Rao, L.; Malviya, L.; Chawla, M.; Parmar, A. MIMO-Array Antenna With Beamforming for 5G Applications. In Proceedings of the 2021 10th IEEE International Conference on Communication Systems and Network Technologies (CSNT), Bhopal, India, 18–19 June 2021; pp. 27–32.
30. Abdulkawi, W.M.; Sheta, A.F.A.; Elshafiey, I.; Alkanhal, M.A. Design of Low-Profile Single-and Dual-Band Antennas for IoT Applications. *Electronics* **2021**, *10*, 2766. [CrossRef]

31. Gangwar, R.K.; Singh, S.P.; Kumar, D. A modified fractal rectangular curve dielectric resonator antenna for WiMAX application. *Prog. Electromagn. Res.* **2010**, *12*, 37–51. [CrossRef]

32. Dhar, S.; Ghatak, R.; Gupta, B.; Poddar, D.R. A wideband Minkowski fractal dielectric resonator antenna. *IEEE Trans. Antennas Propag.* **2013**, *61*, 2895–2903. [CrossRef]

33. Muhsin, M.Y.; Salim, A.J.; Ali, J.K. Compact MIMO Antenna Designs Based on Hybrid Fractal Geometry for 5G Smartphone Applications. *Prog. Electromagn. Res. C* **2022**, *118*, 247–262. [CrossRef]

34. Sharma, N.; Singh, H.S.; Khanna, R. Design and Analysis of Multiband Fractal Antenna for MIMO/Diversity Applications. *Wirel. Pers. Commun.* **2022**, *122*, 3671–3686. [CrossRef]

35. Sheta, A.; Al-Eshaikh, M. A new small size non-degenerate dual-mode patch filter. *J. Electromagn. Waves Appl.* **2011**, *25*, 1504–1514. [CrossRef]

36. Mahmoud, S.F.; Sheta, A.; Alkanhal, M.A.; Alhekail, Z. Analysis and design of compact wide tunable-band antenna based on reactively loaded patch. *Microw. Opt. Technol. Lett.* **2012**, *54*, 884–888. [CrossRef]

37. Sheta, A.; Dib, N.; Mohra, A. Investigation of new nondegenerate dual-mode microstrip patch filter. *IEE Proc. -Microw. Antennas Propag.* **2006**, *153*, 89–95. [CrossRef]

38. Mansour, R.R. Design of superconductive multiplexers using single-mode and dual-mode filters. *IEEE Trans. Microw. Theory Tech.* **1994**, *42*, 1411–1418. [CrossRef]

39. Du, Z.; Gong, K.; Fu, J.; Gao, B. Analysis of microstrip fractal patch antenna for multi-band communication [by FDTD]. *Electron. Lett.* **2001**, *37*, 805–806. [CrossRef]

40. Zhao, L.; Liu, F.; Shen, X.; Jing, G.; Cai, Y.-M.; Li, Y. A high-pass antenna interference cancellation chip for mutual coupling reduction of antennas in contiguous frequency bands. *IEEE Access* **2018**, *6*, 38097–38105. [CrossRef]

41. Yu, K.; Li, Y.; Liu, X. Mutual coupling reduction of a MIMO antenna array using 3-D novel meta-material structures. *Appl. Comput. Electromagn. Soc. J.* **2018**, *6*, 758–763.

42. Jiang, T.; Jiao, T.; Li, Y. A low mutual coupling MIMO antenna using periodic multi-layered electromagnetic band gap structures. *Appl. Comput. Electromagn. Soc. J.* **2018**, *33*, 305–311.

43. Geozandas. Time-Domain Antenna Measurement Systems. Available online: https://geozondas.com/main_page.php?pusl=12 (accessed on 26 July 2022).

44. Shayea, I.; Rahman, T.A.; Azmi, M.H.; Islam, M.R. Real measurement study for rain rate and rain attenuation conducted over 26 GHz microwave 5G link system in Malaysia. *IEEE Access* **2018**, *6*, 19044–19064. [CrossRef]

45. Khalid, M.; Iffat Naqvi, S.; Hussain, N.; Rahman, M.; Mirjavadi, S.S.; Khan, M.J.; Amin, Y. 4-Port MIMO antenna with defected ground structure for 5G millimeter wave applications. *Electronics* **2020**, *9*, 71. [CrossRef]

46. Votis, C.; Tatsis, G.; Kostarakis, P. Envelope correlation parameter measurements in a MIMO antenna array configuration. *Int. J. Commun. Netw. Syst. Sci.* **2010**, *3*, 350. [CrossRef]

47. Liu, F.; Guo, J.; Zhao, L.; Huang, G.-L.; Li, Y.; Yin, Y. Ceramic superstrate-based decoupling method for two closely packed antennas with cross-polarization suppression. *IEEE Trans. Antennas Propag.* **2020**, *69*, 1751–1756. [CrossRef]

48. Roy, S.; Chakraborty, U. Mutual coupling reduction in a multi-band MIMO antenna using meta-inspired decoupling network. *Wirel. Pers. Commun.* **2020**, *114*, 3231–3246. [CrossRef]

49. Saxena, G.; Jain, P.; Awasthi, Y.K. High diversity gain MIMO-antenna for UWB application with WLAN notch band characteristic including human interface devices. *Wirel. Pers. Commun.* **2020**, *112*, 105–121. [CrossRef]

50. Sharawi, M.S. Printed multi-band MIMO antenna systems and their performance metrics [wireless corner]. *IEEE Antennas Propag. Mag.* **2013**, *55*, 218–232. [CrossRef]

51. Kulkarni, J.; Desai, A.; Sim, C.-Y.D. Wideband Four-Port MIMO antenna array with high isolation for future wireless systems. *AEU-Int. J. Electron. Commun.* **2021**, *128*, 153507. [CrossRef]

52. Tariq, S.; Naqvi, S.I.; Hussain, N.; Amin, Y. A Metasurface-Based MIMO Antenna for 5G Millimeter-Wave Applications. *IEEE Access* **2021**, *9*, 51805–51817. [CrossRef]

53. Abouda, A.A.; El-Sallabi, H.M.; Haggman, S. Effect of mutual coupling on BER performance of Alamouti scheme. In Proceedings of the 2006 IEEE Antennas and Propagation Society International Symposium, Albuquerque, NM, USA, 9–14 July 2006; pp. 4797–4800.

54. Gupta, I.; Ksienski, A. Effect of mutual coupling on the performance of adaptive arrays. *IEEE Trans. Antennas Propag.* **1983**, *31*, 785–791. [CrossRef]

55. Wu, Y.; Linnartz, J.P.; Bergmans, J.; Attallah, S. Effects of antenna mutual coupling on the performance of MIMO systems. In Proceedings of the 29th Symposium on Information Theory in the Benelux, Rotterdam, The Netherlands, 11–12 May 2010; pp. 1–8.

56. Van Trees, H.L. *Optimum Array Processing: Part IV of Detection, Estimation, and Modulation Theory*; John Wiley & Sons: New York, NY, USA, 2004.

57. Proakis, J.G.; Salehi, M. *Digital Communications*; McGraw-Hill: New York, NY, USA, 2001; Volume 4.

58. Mathworks. Available online: https://www.mathworks.com/ (accessed on 31 May 2022).